Tracking the ATP-binding response in adenylate kinase in real time

Fredrik Oradd, Harsha Ravishankar, Jack Goodman, Per Rogne, Lars Backman, Annette Duelli, Martin Nors Pedersen, Matteo Levantino, Michael Wulff, Magnus Wolf-Watz, et al.

BIOPHYSICS

Tracking the ATP-binding response in adenylate kinase in real time

Fredrik Orädd[1], Harsha Ravishankar[1]†, Jack Goodman[1]‡, Per Rogne[1], Lars Backman[1], Annette Duelli[2], Martin Nors Pedersen[3]§, Matteo Levantino[3], Michael Wulff[3], Magnus Wolf-Watz[1], Magnus Andersson[1]*

The biological function of proteins is critically dependent on dynamics inherent to the native structure. Such structural dynamics obey a predefined order and temporal timing to execute the specific reaction. Determination of the cooperativity of key structural rearrangements requires monitoring protein reactions in real time. In this work, we used time-resolved x-ray solution scattering (TR-XSS) to visualize structural changes in the *Escherichia coli* adenylate kinase (AdK) enzyme upon laser-induced activation of a protected ATP substrate. A 4.3-ms transient intermediate showed partial closing of both the ATP- and AMP-binding domains, which indicates a cooperative closing mechanism. The ATP-binding domain also showed local unfolding and breaking of an Arg^{131}-Asp^{146} salt bridge. Nuclear magnetic resonance spectroscopy data identified similar unfolding in an Arg^{131}Ala AdK mutant, which refolded in a closed, substrate-binding conformation. The observed structural dynamics agree with a "cracking mechanism" proposed to underlie global structural transformation, such as allostery, in proteins.

INTRODUCTION

Conformational dynamics are inherent to protein structure and are essential for enzymatic transitions. Both local side-chain rearrangements and global large-scale conformational changes contribute to the biological function. A critical component in the orchestration of protein dynamics is the synchronization of structural events according to predefined pathways, in analogy to the moving parts of, e.g., a combustion engine. Examples of such precise coordination of structural dynamics are the unidirectional transport of ions that prevents backflow to build up gradients across biological membranes (*1*) or sugar uptake into membrane protein transporters (*2*). Adenylate kinase (AdK) catalyzes a reversible phosphoryl transfer reaction to produce two adenosine 5′-diphosphate (ADP) molecules from adenosine 5′-triphosphate (ATP) and adenosine 5′-monophosphate (AMP) and thereby plays an important role in cellular energy homeostasis (*3*). AdK has become a principal model system to study relationships between protein structure, conformational dynamics, and catalysis in enzymes (*4*–*14*). However, direct experimental evidence for the coordinated structural rearrangements upon substrate binding is still missing.

AdK is a 23.6-kDa protein that consists of a central domain (CORE) linked to two flexible domains: the AMP-binding domain (NMPbd) and the ATP-binding domain (LIDbd). Crystal structures of the *Escherichia coli* AdK have resolved the apo state, with both NMPbd and LIDbd in open configurations with accessible AMP- and ATP-binding sites [Protein Data Bank (PDB) ID: 4AKE] (*15*) and a closed conformation trapped with a P^1,P^5-bis(adenosine-5′-) pentaphosphate (Ap_5A) inhibitor (PDB ID: 1AKE) (*16*). Thus, the structural information is indicative of large-scale conformational changes associated with substrate binding, i.e., binding of ATP and AMP is associated with closure of the LIDbd and NMPbd, respectively (Fig. 1). Because this observed closing conformational change is at the heart of the substrate-binding mechanism, several experimental and simulation approaches have attempted to determine the kinetics, relative ordering, and level of cooperativity in the domain closing.

In nuclear magnetic resonance (NMR) measurements of the *E. coli* AdK, the substrate-binding domains were measured to close in 0.73 ms (*10*). Because the NMR data were fitted by a single exchange rate, determination of the relative ordering of the LIDbd and NMPbd closing movements was prevented. Single-molecule Förster resonance energy transfer (sm-FRET) experiments observed

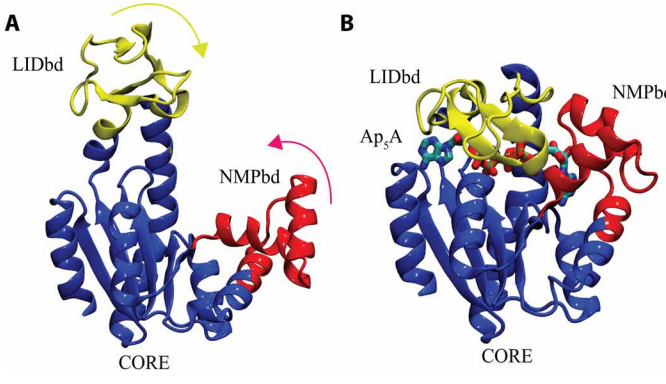

Fig. 1. Open and closed AdK crystal structures with LIDbd (yellow) consisting of residues 118 to 167; CORE (blue) consisting of residues 1 to 29, 68 to 117, and 161 to 214; and NMPbd (red) domains consisting of residues 30 to 67. (**A**) Substrate-free open conformation of AdK (PDB ID: 4AKE), with arrows indicating directions of conformational change to achieve a substrate-bound state. (**B**) Closed conformation (PDB ID: 1AKE), with LID and NMP domains rotated to close over the nonhydrolyzable Ap_5A inhibitor (shown as sticks).

[1]Department of Chemistry, Umeå University, Linnaeus Väg 10, 901 87 Umeå, Sweden. [2]Department of Biomedical Sciences, University of Copenhagen, Blegdamsvej 3, 2200 Copenhagen, Denmark. [3]ESRF—The European Synchrotron, 71 Avenue des Martyrs, CS40220, 38043 Grenoble, Cedex 9, France.
*Corresponding author. Email: magnus.p.andersson@umu.se
†Present address: Laboratory of Metabolism, National Cancer Institute, National Institutes of Health, Bethesda, MD 20892, USA.
‡Present address: Faculty of Health and Applied Science, University of the West of England, Coldharbour Lane, Bristol BS16 1QY, UK.
§Present address: Novo Nordisk A/S, Novo Nordisk Park, DK-2760 Måløv, Denmark.

the open and closed states of the LIDbd to be in equilibrium and that ATP binding shifted the ensemble toward a closed state with closure taking place in 2.3 ms (*4*). These closing dynamics were measured by attaching probes onto the LIDbd and CORE domains, i.e., the NMPbd closing dynamics were not measured. In sm-FRET experiments probing both LIDbd and NMPbd dynamics, a closing time of 0.5 ms was registered (*13*). A similar labeling scheme resulted in a very fast LIDbd-NMPbd closing time of 15 μs onto the substrates (*5*). While sm-FRET experiments can give important insights into protein dynamics and kinetics, such measurements cannot resolve relative structural changes in, e.g., LIDbd-NMPbd closing events and the overall interpretations can be ambiguous given the small number of distance probes. In addition, the placement of probes can affect the monitored dynamics. Therefore, attaching the LIDbd probe onto an extended loop region, which likely displays a wide range of dynamics, can possibly explain the varying LIDbd-NMPbd closing times observed by sm-FRET (*4*, *5*, *13*). In summary, the experimentally measured time scales for closing the substrate-binding domains span a wide temporal range and cannot resolve the level of cooperativity between the domain-closing events.

Computer simulations can sample correlative motion between the NMP and LID domains, which cannot be observed in ensemble-averaged experiments. The consensus of a range of molecular dynamics (MD) simulations is that a lower free-energy barrier is associated with LIDbd closure compared to NMPbd closure, and therefore, LIDbd is predicted to close before NMPbd (*8*, *9*, *17*–*24*). However, both LID-first and NMP-first pathways have been observed (*25*, *26*), and temperature has been implicated to determine which of these pathways are dominating (*27*). Simulations have also suggested that the NMPbd should close first upon ligand binding (*28*). The variance in the observed results can possibly be explained by atomistic MD simulations not being able to sample biological time scales and the usage of coarse-grained models, enhanced sampling methods, and force field accuracies.

Conformational changes in proteins are often key events for generation of a biological response. For instance, the marked wrap-around conformational transition by calmodulin is known to activate plasma membrane Ca^{2+}–ATPases (*29*). For AdK, the massive conformational change in the LIDbd in response to binding of ATP serves several purposes including (i) dehydration of the active site to prevent nonproductive hydrolysis of ATP into ADP and inorganic phosphate (*30*), (ii) completion of the active site by Arg^{156} situated at the top of the NMPbd, and (iii) an optimal alignment of substrates to enable the nucleophilic attack by an oxygen on the α-phosphate of AMP on the γ-phosphate of ATP. The classical model underlying conformational changes is the "induced fit" model (*31*), where a bound ligand induces the conformational change in a protein. This model is dependent on a translational motion of rigid and folded structural elements. An alternative model, denoted the "cracking model," originates from the energy landscape theory (*32*). In this model, conformational transitions have been proposed to involve local unfolding with subsequent refolding of specific protein segments. In essence, the model suggests that the cooperative folding/unfolding mechanism is used by proteins not only for folding of native structures (*33*) but also for conformational transitions between folded structural states. Such a cracking mechanism could possibly constitute a fundamental driving force for transitioning between stable intermediate states in enzymatic reactions. For instance, the kinase domain of the epidermal growth factor receptor has been proposed to use a cracking mechanism for an activating conformational change (*34*). Local regions in a protein can be under considerable elastic stress, which then upon local unfolding is relieved and the structural transition can evolve along the reaction coordinate to a nearby stable point in the free-energy landscape. Using a coarse-grained model and the principle of minimal frustration, localized strain energy and unfolding in the LIDbd was suggested to be the source of conformational change in the AdK reaction (*35*). Mutations that disrupt a hydrophobic cluster in the LIDbd can induce unfolding, which is then followed by refolding in the open-to-closed conformational transition (*12*, *36*). While these observations are in favor of a cracking mechanism, experimental real-time observation of the initial stages of the AdK reaction—that would provide more direct evidence of a cracking mechanism—has so far been elusive.

Time-resolved x-ray solution scattering (TR-XSS) experiments and subsequent structural refinement can track and visualize structural rearrangements in photoactive chemicals (*37*), protein dimerization (*38*), folding (*39*, *40*) and temperature-jump (*41*) processes, as well as large-scale conformational changes in soluble (*42*–*45*) and membrane (*46*–*49*) proteins. A TR-XSS approach has also been proposed to simultaneously track local and global structural rearrangements in a protein (*50*). Recent experiments have explored a molecular switch mechanism in a circular oligomer of the photoactive yellow protein (*51*) and determined the ultrafast structural response (*52*) and salt bridge controlled allostery (*53*) in hemoglobin. The TR-XSS experiments take a pump-and-probe approach to track structural change in real time, where a laser pulse is typically used to trigger the reaction. Therefore, light-sensitive proteins constitute prime targets (*43*–*48*), but caged compounds, such as caged ATP, have also been used to indirectly trigger ATP-dependent proteins (*49*) and processes (*38*). The laser-induced dynamics can, for instance, be registered using synchrotron-generated x-ray pulses capable of delivering 10^{10} photons onto the sample in 100 ps (*54*). Microsecond-long trains of single 100-ps x-ray pulses enhance the signal-to-noise ratio and are ideally suited to track dynamics on the micro- to millisecond biological time scale. The advantage of the TR-XSS methodology is that changes in all interatomic distances are measured simultaneously in real time, which enables direct determination of ordering and cooperativity of structural events. In addition, being a nonintrusive method, there are no risks of disturbing the natural dynamics by, e.g., introducing labeling probes.

In this study, we used TR-XSS to track the conformational dynamics of *E. coli* AdK after laser-induced release of ATP in a sample that contained saturating concentrations of the AMP substrate. During the 20-μs to 25-ms temporal window that we tracked AdK structural dynamics, we observed strong shifts in the difference scattering profiles. Structural refinement of a 4.3-ms transient intermediate state showed the dominating population of protein molecules to display local unfolding in the LIDbd and partial closures of both the LIDbd and the NMPbd. In NMR measurements, an AdK mutant that lacked an Arg^{131}-Asp^{146} salt bridge in the LIDbd showed local unfolding, followed by refolding upon substrate binding. Our conclusion is that access to ATP—in the presence of AMP—triggers local unfolding in agreement with a cracking model and that closing of the LIDbd and NMPbd is a cooperative, synchronized structural event.

RESULTS

Tracking the ATP-binding conformational changes in AdK in real time

To assess the AdK structural response to ATP, we activated the protein using laser-induced release of caged ATP in the presence of the AMP substrate. The structural dynamics in the sample were recorded with the TR-XSS methodology at time points from 20 μs to 25 ms, which cover the broad time scale suggested by different experimental NMR and FRET results (*4*, *6*, *12*, *14*, *55*). After removing difference scattering contributions from heating of the solvent (*42*), caged ATP, negative time delay, and concentration-dependent effects (figs. S1 and S2), the measured time-resolved data contained structural information on AdK conformational changes subsequent to release of ATP. The difference spectra displayed features that evolved over time (Fig. 2A). Already at 20 μs, a negative low **q** feature was observed at 0.05 $Å^{-1}$ that persisted until the final 25-ms time point. The other major component was a peak at 0.12 $Å^{-1}$ that accumulated on a millisecond time scale.

To describe the structural dynamics over time, we modeled the kinetics of the time-resolved x-ray data. Singular value decomposition (SVD) analysis (Materials and Methods) showed that two components could explain the major features in the TR-XSS data. The first SVD component contained the negative low **q** feature that was gradually reduced at time points longer than 1 ms (fig. S3). Similarly, the second major component featured the positive peak at 0.12 $Å^{-1}$ that emerged over time, in particular, at time points longer than 1 ms. A two-state sequential kinetic model represented the data well with a global least-squares fit of $S = 1.0 \times 10^{-6}$ (Fig. 2A). The accompanying spectral decomposition of the time-resolved data resulted in early and late time-independent basis spectra (Fig. 2B). The temporal evolution of the transient intermediate states showed an early-to-late rise time of 4.3 ms (Fig. 2C). Because the early basis spectrum occurred within a similar temporal regime as release of the caged ATP (*56*), we focused on structural refinement of the late basis spectrum.

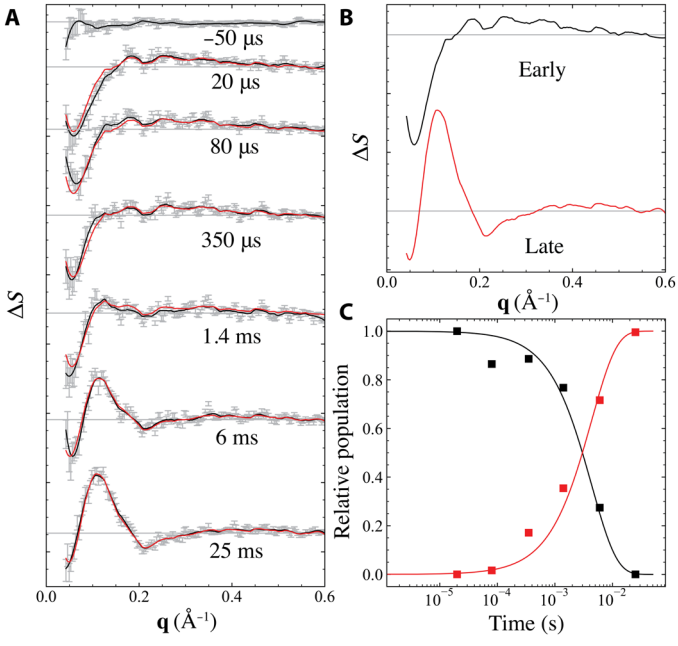

Fig. 2. TR-XSS data of ATP-dependent AdK structural dynamics. (**A**) Difference x-ray scattering data (black) obtained by subtracting x-ray scattering 50 μs before the laser pulse (dark reference) from each time delay. (**B** and **C**) Reconstituted data (red) resulting from linear combination of the population densities and basis spectra are overlaid on the experimental data. (B) Time-independent basis spectra obtained from the spectral decomposition according to a kinetic model including early (black) and late (red) states. (C) Population densities of the early (black) and late (red) transient states as a function of time. The squares show the optimal linear combinations at each individual time point.

Obtaining a structural representation of the 4.3-ms transient intermediate state

To obtain an initial starting point for the structural refinement of the late basis spectrum, we calculated a theoretical difference profile using coordinates of the available *E. coli* AdK crystal structures in open (PDB ID: 4AKE) and closed (PDB ID: 1AKE) conformations (Fig. 3A). While the overall shape of the theoretical difference scattering profile reproduced the shape of the experimental data, there were substantial differences. In particular, the positive feature in the crystal structure data was shifted toward lower **q** values, and the data below 0.2 $Å^{-1}$ differed considerably. A crystallographic *R* factor was calculated to obtain a quantitative measure on the comparison to the experimental data (Materials and Methods). Because thermal fluctuations in a protein were observed to result in *R* factors ~0.1 (*49*), the *R* factor of 0.85 obtained from the comparison to the open and closed crystal structures cannot be considered a satisfactory fit.

To find a better structural solution to the TR-XSS late basis spectrum, and hence to structurally characterize the transient state in the AdK reaction cycle, we used MD simulation to explore equilibrium dynamics in solution. Two simulation trajectories of 450 and 335 ns were generated starting from the open (PDB ID: 4AKE) and closed (PDB ID: 1AKE) *E. coli* AdK crystal structures, respectively. To determine the extent to which the simulations covered AdK dynamics, we calculated root mean square deviation (RMSD) toward the "target" crystal structure, e.g., for the simulation starting from the closed structure, the open structure was used as reference. The LIDbd and NMPbd regions were calculated separately. The obtained RMSD values for the domains were then compared to the average RMSD for the entire protein from both simulations (4.8 Å), which represent thermal fluctuations. In the simulation of the closed state, both the LIDbd and NMPbd visited conformations with similar backbone structure as the open crystal structure (Fig. 3B). The simulation of the open state produced closed conformations of the NMPbd, while the LIDbd remained open. We extracted simulated structures from every nanosecond frame along both trajectories, and their individual theoretical scattering was calculated. To ensure that all possible combinations of degrees of domain closure were taken into account, we generated difference scattering profiles by subtracting scattering from open-closed, closed-open, closed-closed, and open-open simulation frames, generating in total ~600,000 difference scattering profiles and compared to the experimental late basis spectrum (Fig. 3, C to F). It was clear that the difference scattering profiles generated from the closed-state simulation produced most of the satisfactory fits to the experimental data (Fig. 3D). The matrix representation of the *R* factors shows that frames >100 ns produced low *R* factors when paired with the 1- to 100-ns frames. This can be understood by the RMSD plot (Fig. 3B) that shows that the closed structure forms an open state at ~100 ns. The closed-state simulation also generated good fits to the data when combined with the open-state simulation (Fig. 3F), in particular when combining structures from the final 100 ns of the open-state simulation, which

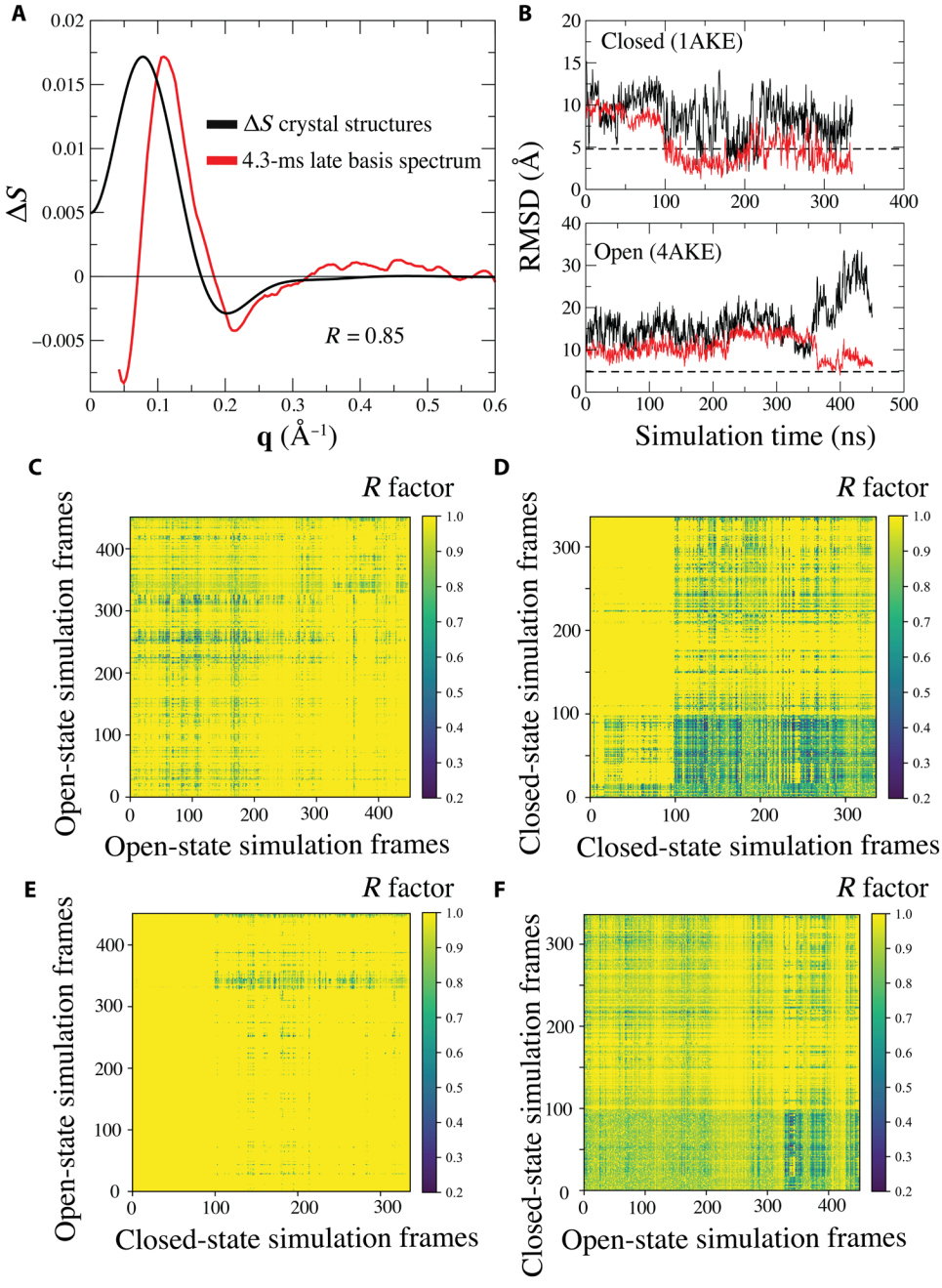

Fig. 3. Structural refinement of the 4.3-ms late basis spectrum. (**A**) Difference x-ray scattering profile calculated from the open (PDB ID: 4AKE) and closed (PDB ID: 1AKE) crystal structures (black) compared to the 4.3-ms late basis spectrum (red) with an *R* factor of 0.85. (**B**) Sampling of domain movements in simulations starting from the closed (top) and open (bottom) crystal structures. The RMSD values measure the convergence of the LIDbd (black) and NMPbd (red) toward the open (top) and closed (bottom) crystal structures. The dashed lines represent the average backbone dynamics displayed by the full protein. *R*-factor matrices calculated from fitting x-ray scattering difference profiles from the (**C**) open-state and open-state, (**D**) closed-state and closed-state, (**E**) open-state and closed-state, and (**F**) closed-state and open-state simulations to the 4.3-ms late basis spectrum. The difference profiles were obtained from structure pairs generated from each frame combination in the simulations.

show a high degree of openness (Fig. 3B), and structures from the 1- to 100-ns frames of the closed-state simulation that featured a closed state. Combinations of structures from the open-state simulation by itself (Fig. 3C) or when reversing the open- and closed-state simulation (Fig. 3E) resulted in fewer fits to the data. Together, this suggests that the late basis spectrum can be explained by conformational changes that are less pronounced compared to those representing full closing events as observed in the crystal structures.

We then extracted the 100 structure pairs that generated the lowest *R* factors from all possible combinations of simulated structures. The structure pairs displayed gradually lowered *R* factors with more pronounced reduction of the 10 best pairs, with *R* factors below 0.24 (Fig. 4A). The 100 lowest *R* factors originated by 60%

from combinations within the closed-state simulation, which was also reflected in the *R*-factor matrices (Fig. 3, C to F). To interpret the structural changes, we generated Cα distance difference matrices. The Cα distance difference matrix based on the open and closed crystal structures identified several regions characterized by domains moving into a closed conformation (fig. S4A). Specifically, four main regions could be discerned corresponding to residues in the ATP-binding LID domain (residues 118 to 167) and AMP-binding NMP domain (residues 30 to 67) to undergo inward rotations in the order of 10 to 25 Å with respect to the CORE domain (residues 1 to 29, 68 to 117, and 161 to 214). To describe the structural ensemble that best agreed with the experimental data, we extracted the 10 pair structures with the lowest *R* factors (Fig. 4A) and calculated an average Cα distance difference matrix (Fig. 4B). The change in distances showed a closing movement of the LIDbd, although much weaker, indicating a partial closure in an inward-rotational movement. Similarly, the matrix showed partial closure of the NMPbd, which indicates that substrate-induced domain closing in AdK is cooperative. The average Cα distance difference matrix representing the 10 highest *R* factors was completely different with structural movements in the opposite directions (Fig. 4C). While the difference scattering profiles that yielded the 10 lowest *R* factors showed excellent agreement to the experimental data at 4.3 ms, the 10 worst difference profiles did not capture the spectral features (Fig. 4D). In addition, while the low *R* structural solutions displayed a relatively small structural variance, the high *R* structures were spread across a wider range of conformations (fig. S4B). Thus, the 4.3-ms time-resolved data could be explained by an ensemble of structures that had initiated closing of both the LIDbd and NMPbd in a cooperative mechanism triggered by the released ATP.

Local unfolding accompanies the closure of the LIDbd

The interdomain dynamics within the LIDbd were different compared to the Cα distance difference matrix for the open and closed crystal structures (compare Fig. 4B and fig. S4A). To identify whether the observed dynamics were possibly associated with breaking of secondary structure suggested to facilitate structural transition in AdK (*32*, *45*, *46*), we tracked the degree of secondary structure throughout the simulations. The region including residues 115 to 155 was involved in notable changes in secondary structure including α-helical and β-sheet unfolding in the open-state simulation (Fig. 5A) and, to a lesser extent, in the closed-state simulation (Fig. 5B). In contrast, both the NMPbd and CORE regions showed conserved secondary structure in both simulations (fig. S5). A possible source for the unfolding dynamics is the Arg^{131}-Asp^{146} salt bridge, which is present in both the open and closed AdK crystal structures (Fig. 5C and fig. S6) and thus constitutes a putative site of stabilization for both these structural intermediate states. To probe the presence

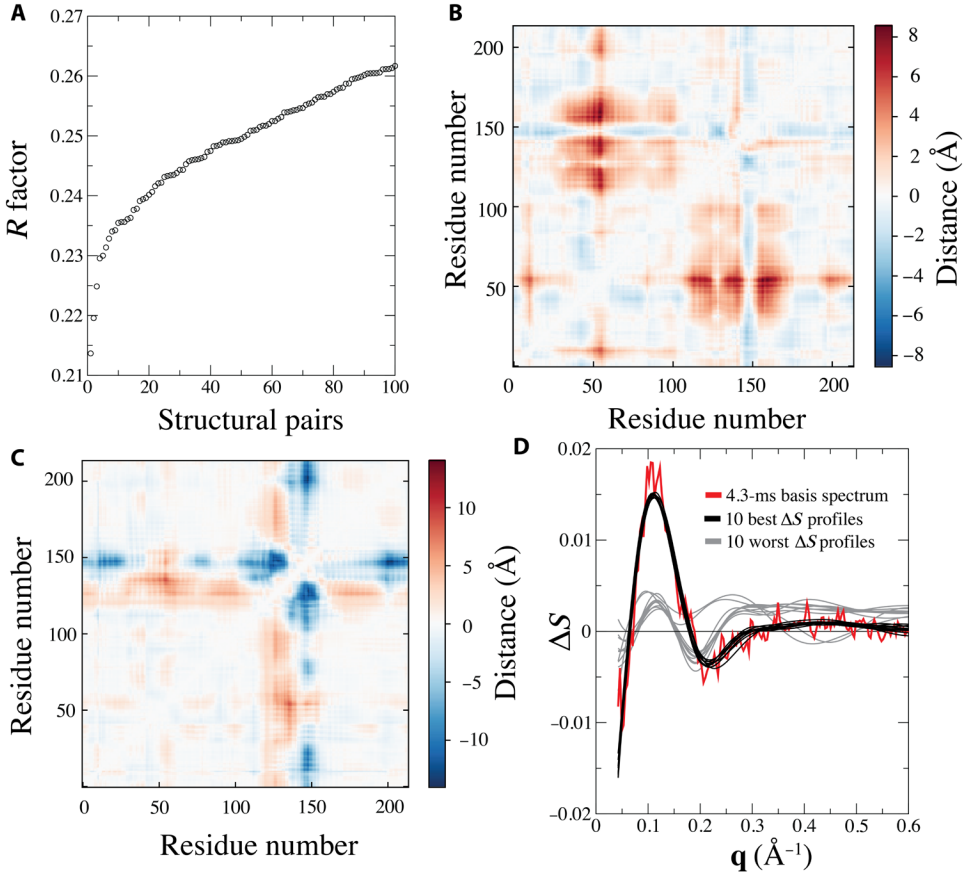

Fig. 4. Structural characterization of the 4.3-ms late basis spectrum. (**A**) *R* factors of 100 structure pairs, with the lowest-scoring *R* factors, generated from all possible combinations of frames from the two simulations. Difference distance matrix averaged across the 10 structure pairs with the (**B**) lowest and (**C**) highest *R* factors. (**D**) Difference x-ray scattering profiles corresponding to the 10 lowest (black) and gray (magenta) *R* factors and the 4.3-ms late basis spectrum (red).

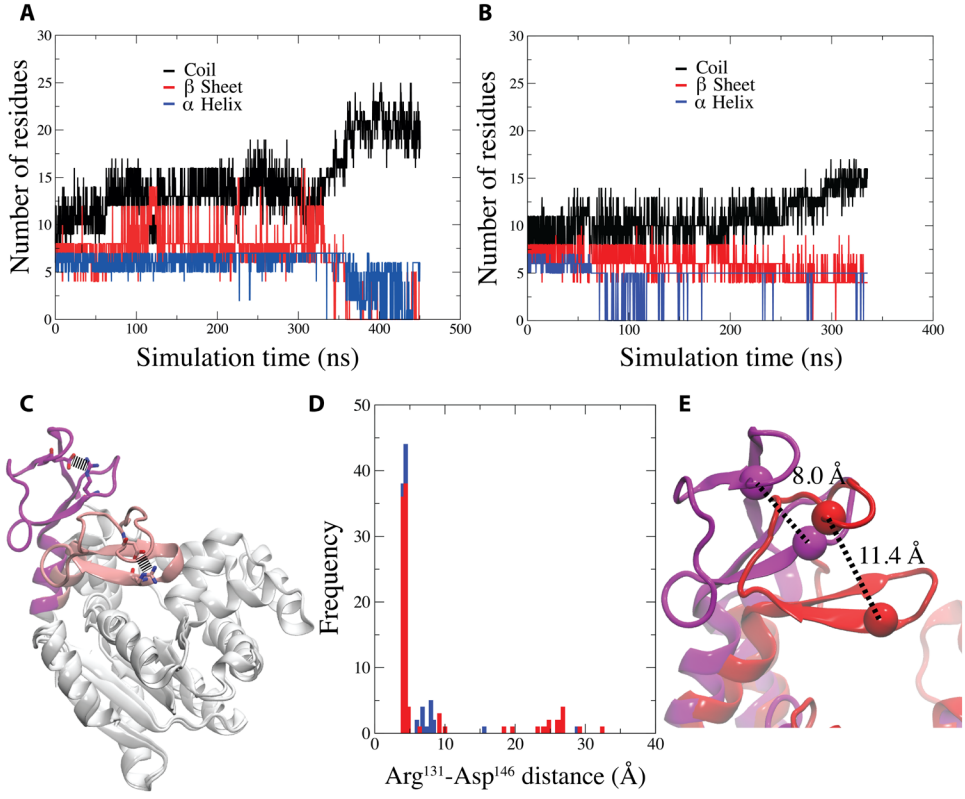

Fig. 5. Structural unfolding dynamics in the LIDbd region. Secondary structure of the LIDbd in the simulations of the (**A**) open and (**B**) closed AdK states. Random coil, β-sheet, and α-helix secondary structures displayed as black, red, and blue lines, respectively. (**C**) Arg^{131}-Asp^{146} salt bridge depicted in sticks and a connecting dashed line in the open and closed AdK crystal structures. The LIDbd region in the open and closed structures is colored magenta and pink, respectively, with the remaining structure in white. (**D**) Histogram depicting the Arg^{131}-Asp^{146} distances measured by the most distal carbon atoms in the respective side chains for the best-fitting 100 structure pairs displayed in blue (ground states) and red (excited states). (**E**) LIDbd region of an average structure from the 10 best-fitting simulated excited states (red), with Arg^{131} and Asp^{146} Cα atoms shown as van der Waals spheres compared to the open-state crystal structure (magenta).

of a broken salt bridge, the Arg^{131}-Asp^{146} inter-residue distance was tracked in simulated structures corresponding to excited states (red columns, Fig. 5D) and ground states (blue columns, Fig. 5D). The 100 lowest *R*-factor structural ensemble contained structures with a broken Arg^{131}-Asp^{146} salt bridge (Fig. 5D). The average structure corresponding to 10 structures from the excited state of the pair showed unfolding and a separation of the β-sheet motif toward a partially closed conformation (red structure, Fig. 5E).

To further explore the structural and functional role of the Arg^{131}-Asp^{146} salt bridge experimentally, we constructed an Arg^{131}Ala AdK mutant. The 576 ± 30 nM binding affinity (K_d) to the Ap_5A inhibitor measured by isothermal titration calorimetry was in a similar range as for the wild-type (WT) protein (354 ± 72 nM) (table S1 and fig. S7). In addition, the catalytic parameters (K_M and k_{cat}) from a coupled ATPase assay (Materials and Methods) also showed a high degree of similarity (table S1). Overall, the Arg^{131}Ala mutant displayed a marginal reduction of the binding affinity and k_{cat}, in particular when compared in terms of free-energy differences (table S1). Given these functional data, only marginal effects on the structure of the substrate-free enzyme would be expected. However, as evident from a ^1H-^{15}N heteronuclear single-quantum coherence (HSQC) NMR spectrum, the structural effect was substantial and a large set of amino acids in the LIDbd becomes unfolded as manifested by a loss of resonances (Fig. 6A). Thus, a loss of the Arg^{131}-Asp^{146} salt bridge resulted in partial unfolding of the AdK mutant. In addition, the ^1H-^{15}N HSQC spectrum of the Arg^{131}Ala AdK structure in the presence of the inhibitor Ap_5A showed that the unfolded segment is now folded (Fig. 6B). The fact that binding and catalysis in the Arg^{131}Ala mutant are only slightly affected and that the LIDbd, at the same time, is partially unfolded is consistent with the proposed cracking model (*32*).

In summary, our data show that upon access to the ATP substrate in the presence of AMP, the initial 4.3-ms state is defined by breakage of the Arg^{131}-Asp^{146} salt bridge and the resulting unfolding of secondary structure in the LIDbd to induce a partial closing movement upon the ATP substrate (Fig. 7). In addition, while devoid of unfolding events, the NMPbd also undergoes partial closing, indicating that the substrate-induced closing response in AdK involves cooperativity between the two domains.

DISCUSSION

In this work, we tracked the initial ATP-triggered structural response of AdK in real time and observed unfolding and partial closure of the substrate-binding domains. Although the NMP substrate was present in the sample, the NMPbd remained in an open position. Hence, both substrates are required to initiate the closing mechanism. The observed cooperativity between the LIDbd and NMPbd

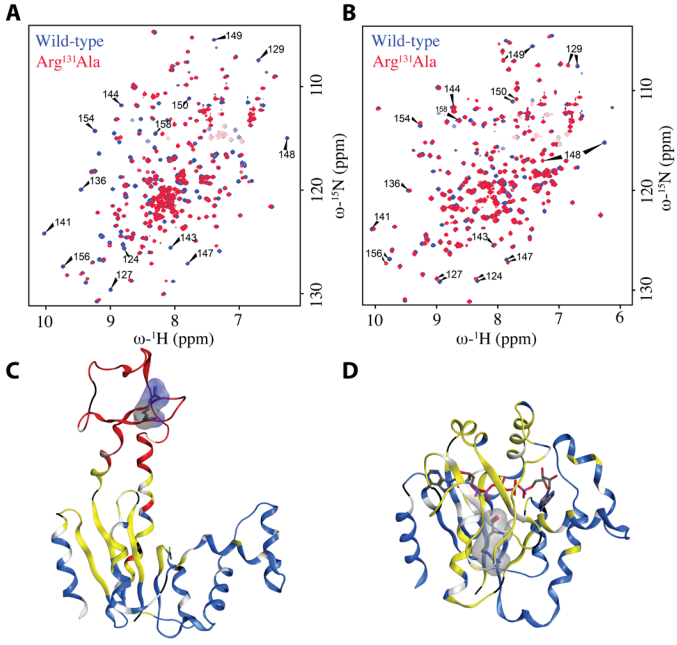

Fig. 6. Ap_5A-mediated folding of the LIDbd in an $Arg^{131}Ala$ AdK mutant. (**A**) ^1H-^{15}N HSQC spectra of substrate-free $Arg^{131}Ala$ (red) and WT (blue) AdK show multiple missing residues in the LIDbd because of local unfolding in the $Arg^{131}Ala$ variant. (**B**) Residues that are missing in ^1H-^{15}N HSQC spectra of substrate-free $Arg^{131}Ala$ are visible in the Ap_5A complex and appear at chemical shifts close to those of the WT (blue), demonstrating that these residues undergo a coupled folding and binding reaction induced by Ap_5A. Visualization of chemical shift differences between (**C**) $Arg^{131}Ala$ and WT AdK in substrate-free and (**D**) Ap_5A-saturated (right) states with $Arg^{131}Ala$ resonances that are either missing (red), substantially shifted (yellow), or only slightly shifted (blue) displayed on the open and closed AdK crystal structures. ppm, parts per million.

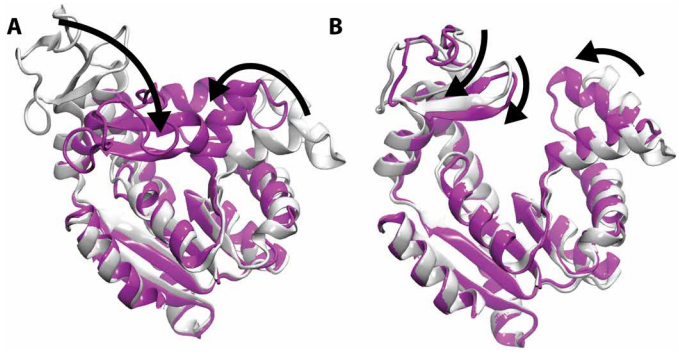

Fig. 7. TR-XSS models show the early stages of AdK activation. (**A**) Open (white) and closed (magenta) crystal structures. (**B**) Structure pair corresponding to averages of the 10 lowest *R*-factor pairs (ground and excited structures depicted in white and magenta, respectively). Arrows indicate the direction of the conformational change. All structures were aligned on the CORE region (residues 1 to 29, 68 to 117, and 161 to 214).

upon binding of substrates was also seen in NMR measurements that showed ATP binding to induce structural change also in the NMP domain (*6*), which indicate the existence of a communicative network spanning between the LIDbd and NMPbd. Such networks can be activated by an inherent trigger, such as, e.g., protonation state in the lactose permease membrane transporter (*57*). Similarly, ATP binding could act as a trigger to activate cooperativity in AdK. A possible molecular explanation has been suggested by Daily *et al.* (*19*): Binding of ATP creates more stabilizing contacts between the LIDbd and the CORE compared to what AMP binding can induce in terms of NMPbd-CORE contacts.

The TR-XSS methodology is optimal for tracking conformational dynamics in real time and determines cooperativity and ordering of structural events (*58*). To obtain a measurable signal, a large population of protein molecules needs to be triggered to synchronize their functional conformation dynamics in time. Hence, an efficient trigger is a prerequisite for TR-XSS measurements, and traditionally, laser activation has been used. For this reason, photoactive chemicals (*37*) and proteins (*38*, *42*–*45*, *47*, *48*, *59*–*61*) that can be directly activated by the laser pulse are common TR-XSS targets. However, indirect triggering by activation of caged compounds, such as ATP (*38*, *49*, *62*, *63*), neurotransmitters (*64*), and ions (*65*), constitutes a means of drastically increasing the number of possible targets for TR-XSS characterization. In this study, we used activation of caged ATP to indirectly trigger the ATP-dependent AdK enzyme. Caged ATP releases on the millisecond time scale (*56*), which overlaps with the observed faster dynamics (early state) and hence limited our characterization to the 4.3-ms late state intermediate. Because free ATP continues to be released during the experiment, we are limiting the study to observe the initial structural response to the ATP substrate, which builds up with time as the late basis spectrum. Grouping the difference scattering signal into caged ATP related (early state) and protein dynamics related (late state) was further justified by the SVD analysis that showed two major components, with the second component being more or less identical to the late basis spectrum (fig. S3).

Being time-resolved measurements, the difference scattering profiles correspond to pairs of structures, where one represents the protein before ATP release (prepulse state) and the other corresponds to the protein in the presence of ATP (excited state). The 10 excited states that were in best agreement with the experimental data showed structures with partially closed LIDbd and NMPbd, with the LIDbd being partly unfolded. This seemingly contradicts computer simulation results that show ATP or AMP presence to close the respective binding domain (*66*). However, NMR experiments have shown that neither of the NMP nor LID domain is fully closed in the presence of a single ATP or AMP (*6*). Our results show that the prepulse state, i.e., AdK in the presence of AMP, displays open conformations of both LIDbd and NMPbd, such as was observed in sm-FRET studies on AdK in the absence of substrates (*5*). It is not until presented with the ATP substrate that the protein reaction is initiated by local unfolding in the LIDbd and concerted closing of both the LIDbd and NMPbd.

It is well established that the AdK enzyme samples both closed and open conformations in the absence of substrates (*13*). Our results are not in disagreement with these observations because we are measuring a structural response from the majority of the population upon release of ATP, i.e., the proteins likely need to reach a certain level of openness until they can bind ATP, and therefore, closing dynamics are triggered successively over time. This is reflected in the RMSD spread of the low-*R* structural solutions (fig. S4B). It has been argued that allosteric structural changes not necessarily need to visit a single transition state but can rather pass through a transition-state ensemble of structures that are partially

unfolded (*32*). Therefore, the 10 excited states that were in best agreement with the experimental data might correspond to such a transition-state ensemble. Dissecting the ensemble based on an inter-residue distance yielded structures with successively varying degrees of the same overall structural change (Fig. 5D).

The local unfolding or cracking observed in the 4.3-ms TR-XSS intermediate structure agrees with a proposed mechanism that requires loss of structural strain to enable funneling through the free-energy landscape to the next stable intermediate state (*32*). Because the Arg^{131}-Asp^{146} salt bridge was observed to break in structures of the transition-state ensemble but was present in both the open and closed AdK crystal structures, we putatively assigned this salt bridge a role for triggering the local unfolding. NMR measurements showed an Arg^{131}Ala AdK mutant to display substantial unfolding in the LIDbd in the absence of substrates, which refolded upon binding the inhibitor Ap_5A. However, we did not observe unfolding near Pro^{177} as has been suggested by Brokaw and Chu (*9*). Hence, the LIDbd closes from the outside in, similar to predictions from MD simulations where the β-sheet loop was observed to move toward the CORE region (*22*).

The communicative network dynamics underlying the observed cooperativity can be divided into two fundamentally different substrate-binding mechanisms, induced fit and conformational selection. In the induced fit–binding mechanism, the ligand binds to the protein in an open conformation before closure. In the conformational selection binding, the protein can also close in the absence of the substrate, but the presence of the substrate shifts the population toward the closed conformation. Earlier studies of AdK have shown evidence for both induced fit (*28*, *35*, *67*) and conformational selection (*14*, *18*, *27*). The TR-XSS data presented here determined cooperativity in the domain closure, which might be considered an induced fit mechanism. However, because we are measuring an ensemble of structures over time, it is also possible that we are observing a shift in the fast open-closed events toward closed states representative of a conformational selection mechanism. It has been argued that AdK likely uses both mechanisms (*55*).

Last, the observed local unfolding and partial closure of the LIDbd must somehow be triggered by binding of the ATP. Such ultrafast dynamics traveling through communicative networks have been referred to as a protein quake (*68*). X-ray free-electron laser (XFEL) technology has enabled visualization of protein quakes in, e.g., photosynthetic reaction center (*69*) and myoglobin (*70*,*71*) proteins as release of strain along propagation pathways on the femto- to picosecond time scale. Hence, XFEL experiments, together with fast-release caged ATP (*72*), can also possibly enable tracking the structural signal from ATP binding to the local unfolding event and closing of the LIDbd in AdK. Uncovering such ultrafast, collective dynamics along with the slower larger-scale structural rearrangements detected in this work holds promise to provide better understanding of the communicative networks underlying allostery in proteins.

MATERIALS AND METHODS

AdK preparation

The gene for the arginine-131 to alanine mutant (Arg^{131}Ala) was synthesized and cloned into a self-inducing plasmid (Eurofins Genomics, Germany), pEAK91-R131A. Both pEAK91 (WT) and pEAK91-R131A (Arg^{131}Ala) were transformed into *E. coli* BL21(DE3) cells and cultivated in M9 minimal media, with $^{15}NH_4Cl$ as the sole source of nitrogen to ^{15}N-label the protein for NMR applications. The two variants were purified according to an established protocol (*14*). The NMR spectra were acquired on a 200 μM sample of either WT or Arg^{131}Ala in 50 mM NaCl and 30 mM MES (pH 6.0). For spectra of Ap_5A-bound AdK, 2 mM Ap_5A was added. All NMR samples contained 7% D_2O to provide a lock signal for the spectrometer. The sample for the TR-XSS experiment was prepared by mixing the AdK protein to a final concentration of 25 mg/ml protein with 50 mM NaCl, 30 mM Mops-KOH (pH 7.0), 2 mM AMP, 2 mM $MgCl_2$, and 10 mM nitrophenylethyl ester (NPE)–caged ATP (final concentration).

TR-XSS data collection

The TR-XSS experiments were performed at the dedicated time-resolved beamline ID09 at the European Synchrotron Radiation Facility (ESRF) at Grenoble, France (*73*). The AdK sample was pumped at a constant flow rate of 41.7 μl/min through a 300-μm quartz capillary (Hampton Research), replenishing the sample every 10-Hz repetition cycle. NPE-caged ATP in the sample was photolyzed with a nanosecond laser source at 1 mJ/mm^2, exhibiting an elliptical 1 mm × 0.25 mm beam shape directed onto the spot on the capillary that was probed by the pulsed x-ray beam. The dimensions of the x-ray beam were 60 μm × 100 μm generated by polychromatic undulator radiation with an energy dispersion of $\Delta E/E$ = 3% and a peak energy of 18 keV. The sample-to-detector distance was 400 mm, and a helium-filled conical chamber was placed in-between the sample and the detector to reduce the background scattering. X-ray pulses of 20 μs were isolated from the synchrotron in a multibunch mode using a high-speed rotating chopper (*74*). The temperature in the experimental hutch was 294 K.

To avoid experimental drift in the measurements, time delays were measured in a predefined order and interspersed with a negative time delay after two time delays: −50 μs, 80 μs, 1.4 ms, −50 μs, 350 μs, 25 ms, −50 μs, 6 ms, and 20 μs. Hence, the resulting time series was 20 μs, 80 μs, 350 μs, 1.4 ms, 6 ms, and 25 ms. The scattering intensity from the 20-μs x-ray pulses was recorded on a charge-coupled device camera, with 40 pulses accumulated before detector readout. The measurements were repeated >25 times for each time point, and the difference scattering profiles were averaged from >1000 experiments to obtain a satisfactory signal-to-noise ratio. The experiments were performed at a 10-Hz repetition rate to ensure that the sample was completely replenished between cycles. Because the calculated TR-XSS data also contain the solvent response to heating, the effects were removed according to a previously described protocol (fig. S1) (*42*). We also corrected for subtle features originating from caged ATP and the negative time delay, with limited effects on the basis spectrum profile (fig. S1). X-ray solution scattering profiles can show concentration effects at low **q** values (*75*). A Guinier plot showed low **q** data to deviate from linearity (fig. S2A). We therefore omitted these data points, which constituted ~3% of the data.

Data reduction

The recorded XSS images were radially integrated to obtain intensity curves $S(\mathbf{q}, \Delta t)$ as a function of the magnitude of the scattering vector $\mathbf{q} = 4\pi\sin\theta/\lambda$, where 2θ is the angle of deflection, λ is the x-ray wavelength, and Δt is the time delay between the photoactivating laser and arrival of the x-ray beam. The time-resolved spectra were subtracted from −50-μs "dark" references after alignment in a **q** region of 2.0 to 2.1 $Å^{-1}$, where minimal differences arising from

thermal effects are expected. Difference data that diverged by more than 3.5 times the SD for the given time delay were removed from the dataset before further analysis. This led to ~90% of the data for each time point being retained. The obtained difference scattering curves contain only the signals emerging from protein dynamics.

Spectral decomposition

The AdK difference scattering data from 0 to 0.6 $Å^{-1}$ were spectrally decomposed according to a sequential two-state kinetic model

$$\text{Early} \xrightarrow{k_1} \text{Late}$$

where the rate constant k_1 corresponds to the formation of a transient state. The kinetic model assumes irreversibility and that the early state forms concomitantly with the laser pulse. To obtain the time-independent basis spectra and associated rate constant, spectral decomposition with global fitting was performed on the AdK difference scattering data $\Delta S(\mathbf{q}, \Delta t)$ according to the following equation

$$\Delta S(\mathbf{q}, \Delta t)_{\text{theory}} = U(\mathbf{q})\, C(\Delta t) \quad (1)$$

where $U(\mathbf{q})$ are the basis spectra in the kinetic model and $C(\Delta t)$ describes the time-dependent concentration of the spectral components. The latter is given by the integrated rate equations

$$[\text{Early}] = e^{-k_1 t} \quad (2)$$

$$[\text{Late}] = 1 - e^{-k_1 t} \quad (3)$$

The rate constant was optimized by a global least-squares refinement between the experimental and reconstituted data. To evaluate whether the kinetic model adequately described the experimental data, linear combinations of the basis spectra and population densities were fitted to the experimental difference data. A $\mathbf{q}$ range up to 0.6 $Å^{-1}$ was selected for the structural refinement analyses because it contained most of the spectral features. The resulting basis spectra were subjected to a 21-point smoothening to cancel out experimental noise.

SVD analysis

The TR-XSS dataset was arranged into an $m \times n$ matrix composed of difference scattering intensities recorded at 161 (m) $\mathbf{q}$ values and 6 (n) time points and subjected to singular SVD according to the following equation

$$\Delta S(\mathbf{q}, \Delta t) = U(\mathbf{q})\, S_v\, V(\Delta t)^T \quad (4)$$

Here, $U(\mathbf{q})$ is an $m \times m$ matrix with the orthonormal basis spectra of the dataset ΔS, S_v is an $m \times m$ diagonal matrix indicating the contributions of the basis spectra (singular values), and $V(\Delta t)$ is an $n \times n$ matrix describing the time-dependent variation of the basis spectra.

Structural refinement

Theoretical difference scattering curves were calculated using the software CRYSOL incorporating the solvent correction and boundary layer (*76*). The resulting calculated difference scattering profiles were corrected for the use of polychromatic radiation by mathematical convolution with the measured undulator spectrum. An R factor was defined to measure the fit between the difference XSS curves calculated from structural models and the experimental data in the 0 $Å^{-1} < \mathbf{q} < 0.6$ $Å^{-1}$ range

$$R = \frac{\Sigma\sqrt{(c \times \Delta S^{\text{theory}} - c \times \Delta S^{\text{experiment}})^2}}{\Sigma\sqrt{(\Delta S^{\text{experiment}})^2}} \quad (5)$$

Here, $\Delta S^{\text{experiment}}$ represents a difference XSS basis spectrum from the spectral decomposition of the experimental data, ΔS^{theory} represents a calculated difference XSS curve from a given structural model, and c is a scaling factor.

MD simulations

The AdK simulation systems for the AdK open (PDB ID: 4AKE) and closed (PDB ID: 1AKE) states were built using CHARMM-GUI (*77*) for the Gromacs 2016.4 simulation engine (*78*). Force field parameters were described by the CHARMM36 Additive Force Field (*79*). Each simulation system was energy-minimized in a 5000-step steepest-descent energy minimization followed by a 25-ps NVT equilibration with restraints on protein heavy atoms. In the equilibration simulation, a 1-fs time step was used and a temperature of 303.15 K was maintained using a Nose-Hoover temperature-coupling scheme (*80*, *81*).

The protein conformations used in the structural refinement protocol were produced in 450- and 335-ns unrestrained simulations for the open and closed crystal structures, respectively. In these simulations, a 2-fs time step was used and the temperature was kept at 303.15 K with a Nose-Hoover thermostat (*80*, *81*) and a Parrinello-Rahman semi-isotropic barostat (*82*). Protein structures from every nanosecond frame in each trajectory were extracted, and theoretical scattering profiles were calculated. Difference scattering profiles were then generated by taking each possible combination from the open-closed, closed-open, open-open, and closed-closed simulation frames. The resulting difference scattering profiles were then compared against the 4.3-ms late basis spectrum, and R factors were calculated.

Isothermal calorimetry and ATP activity assay

The Ap_5A binding to the Arg^{131}Ala AdK mutant was determined by isothermal calorimetry using MicroCal iTC_{200} (GE Healthcare Life Science, Little Chalfont, UK), with the measuring cell containing 218 mM WT AdK or 50 μM Arg^{131}Ala AdK in a buffer consisting of 50 mM NaCl and 30 mM Mops at pH 7.0, and the syringe was filled with 0.25 or 0.50 mM Ap_5A in the same buffer. All measurements were done at 298 K. Data analysis was performed with Sedphat (*83*).

The AdK activity was determined using a coupled enzymatic assay (*84*), where the consumption of ATP is coupled to the conversion of NADH [reduced form of nicotinamide adenine dinucleotide (NAD^+)] to NAD^+, which can be spectrophotometrically monitored at 340 nm. The activity assay was performed in a 100 mM tris buffer supplemented with 80 mM KCl. The concentration of ATP was varied between 5 μM and 1.5 mM, and the enzyme concentration was 15 nM. The determined reaction rates (V) as a function of the substrate concentration ([S]) were fitted to the Michaelis-Menten equation

$$V([S]) = \frac{V_{\max} \times [S]}{K_M + [S]} \quad (6)$$

where V_{max} is the maximum reaction rate and K_M is the Michaelis-Menten constant. The curve fitting was performed with Origin (OriginLab Corp., USA). k_{cat} was calculated by normalizing V_{max} with the enzyme concentration [E] (Eq. 7)

$$k_{cat} = \frac{V_{max}}{[E]} \quad (7)$$

NMR measurements

The NMR spectra were acquired using an 850-MHz Bruker Avance III spectrometer equipped with a 5-mmHCN cryoprobe. The experiments were performed at 298 K, using a ^{1}H-^{15}N HSQC pulse sequence with a water-suppressing "Watergate" sequence, recording 2048 × 256 points with a sweep width of 11,111 × 2585 Hz in the ^{1}H and ^{15}N dimensions, respectively. Each line was an average of eight scans. The spectra were acquired, processed, and analyzed using the Topspin 3.6 software. The backbone assignments of WT AdK have previously been published, in both the apo state (*85*) and the Ap_5A-bound state (*86*). For the $Arg^{131}Ala$ AdK variant, 131 of the 181 ^{1}H-^{15}N HSQC resonances overlapped with WT. For the experiment in the presence of the Ap_5A inhibitor, 183 of 184 HSQC resonances overlapped with WT. Amino acid residues with resonances not overlapping enough to be assigned with reasonable certainty were left unassigned.

SUPPLEMENTARY MATERIALS

Supplementary material for this article is available at https://science.org/doi/10.1126/sciadv.abi5514

View/request a protocol for this paper from *Bio-protocol*.

REFERENCES AND NOTES

1. M. Dyla, S. Basse Hansen, P. Nissen, M. Kjaergaard, Structural dynamics of P-type ATPase ion pumps. *Biochem. Soc. Trans.* **47**, 1247–1257 (2019).
2. H. R. Kaback, A chemiosmotic mechanism of symport. *Proc. Natl. Acad. Sci. U.S.A.* **112**, 1259–1264 (2015).
3. P. Dzeja, A. Terzic, Adenylate kinase and AMP signaling networks: Metabolic monitoring, signal communication and body energy sensing. *Int. J. Mol. Sci.* **10**, 1729–1772 (2009).
4. J. A. Hanson, K. Duderstadt, L. P. Watkins, S. Bhattacharyya, J. Brokaw, J. W. Chu, H. Yang, Illuminating the mechanistic roles of enzyme conformational dynamics. *Proc. Natl. Acad. Sci. U.S.A.* **104**, 18055–18060 (2007).
5. H. Y. Aviram, M. Pirchi, H. Mazal, Y. Barak, I. Riven, G. Haran, Direct observation of ultrafast large-scale dynamics of an enzyme under turnover conditions. *Proc. Natl. Acad. Sci. U.S.A.* **115**, 3243–3248 (2018).
6. J. Aden, M. Wolf-Watz, NMR identification of transient complexes critical to adenylate kinase catalysis. *J. Am. Chem. Soc.* **129**, 14003–14012 (2007).
7. M. D. Daily, L. Makowski, G. N. Phillips Jr., Q. Cui, Large-scale motions in the adenylate kinase solution ensemble: Coarse-grained simulations and comparison with solution X-ray scattering. *Chem. Phys.* **396**, 84–91 (2012).
8. Y. Zheng, Q. Cui, Multiple pathways and time scales for conformational transitions in apo-adenylate kinase. *J. Chem. Theory Comput.* **14**, 1716–1726 (2018).
9. J. B. Brokaw, J. W. Chu, On the roles of substrate binding and hinge unfolding in conformational changes of adenylate kinase. *Biophys. J.* **99**, 3420–3429 (2010).
10. M. Wolf-Watz, V. Thai, K. Henzler-Wildman, G. Hadjipavlou, E. Z. Eisenmesser, D. Kern, Linkage between dynamics and catalysis in a thermophilic-mesophilic enzyme pair. *Nat. Struct. Mol. Biol.* **11**, 945–949 (2004).
11. S. Esteban-Martin, R. B. Fenwick, J. Aden, B. Cossins, C. W. Bertoncini, V. Guallar, M. Wolf-Watz, X. Salvatella, Correlated inter-domain motions in adenylate kinase. *PLOS Comput. Biol.* **10**, e1003721 (2014).
12. U. Olsson, M. Wolf-Watz, Overlap between folding and functional energy landscapes for adenylate kinase conformational change. *Nat. Commun.* **1**, 111 (2010).
13. K. A. Henzler-Wildman, V. Thai, M. Lei, M. Ott, M. Wolf-Watz, T. Fenn, E. Pozharski, M. A. Wilson, G. A. Petsko, M. Karplus, C. G. Hubner, D. Kern, Intrinsic motions along an enzymatic reaction trajectory. *Nature* **450**, 838–844 (2007).
14. M. Kovermann, J. Aden, C. Grundstrom, A. E. Sauer-Eriksson, U. H. Sauer, M. Wolf-Watz, Structural basis for catalytically restrictive dynamics of a high-energy enzyme state. *Nat. Commun.* **6**, 7644 (2015).
15. C. W. Muller, G. J. Schlauderer, J. Reinstein, G. E. Schulz, Adenylate kinase motions during catalysis: An energetic counterweight balancing substrate binding. *Structure* **4**, 147–156 (1996).
16. C. W. Muller, G. E. Schulz, Structure of the complex between adenylate kinase from Escherichia coli and the inhibitor Ap5A refined at 1.9 Å resolution. A model for a catalytic transition state. *J. Mol. Biol.* **224**, 159–177 (1992).
17. H. Lou, R. I. Cukier, Molecular dynamics of apo-adenylate kinase: A principal component analysis. *J. Phys. Chem. B* **110**, 12796–12808 (2006).
18. K. Arora, C. L. Brooks III, Large-scale allosteric conformational transitions of adenylate kinase appear to involve a population-shift mechanism. *Proc. Natl. Acad. Sci. U.S.A.* **104**, 18496–18501 (2007).
19. M. D. Daily, G. N. Phillips Jr., Q. Cui, Many local motions cooperate to produce the adenylate kinase conformational transition. *J. Mol. Biol.* **400**, 618–631 (2010).
20. Y. Wang, L. Makowski, Fine structure of conformational ensembles in adenylate kinase. *Proteins* **86**, 332–343 (2018).
21. C. Ye, C. Ding, R. Ma, J. Wang, Z. Zhang, Electrostatic interactions determine entrance/release order of substrates in the catalytic cycle of adenylate kinase. *Proteins* **87**, 337–347 (2019).
22. M. S. Liu, B. D. Todd, R. J. Sadus, Allosteric conformational transition in adenylate kinase: Dynamic correlations and implication for allostery. *Aust. J. Chem.* **63**, 405–412 (2010).
23. B. Jana, B. V. Adkar, R. Biswas, B. Bagchi, Dynamic coupling between the LID and NMP domain motions in the catalytic conversion of ATP and AMP to ADP by adenylate kinase. *J. Chem. Phys.* **134**, 035101 (2011).
24. D. Li, M. S. Liu, B. Ji, Mapping the dynamics landscape of conformational transitions in enzyme: The adenylate kinase case. *Biophys. J.* **109**, 647–660 (2015).
25. O. Beckstein, E. J. Denning, J. R. Perilla, T. B. Woolf, Zipping and unzipping of adenylate kinase: Atomistic insights into the ensemble of open<-->closed transitions. *J. Mol. Biol.* **394**, 160–176 (2009).
26. J.-W. Chu, G. A. Votha, Coarse-grained free energy functions for studying protein conformational changes: A double-well network model. *Biophys. J.* **93**, 3860–3871 (2007).
27. Y. Wang, L. Gan, E. Wang, J. Wang, Exploring the dynamic functional landscape of adenylate kinase modulated by substrates. *J. Chem. Theory Comput.* **9**, 84–95 (2013).
28. Y. Matsunaga, H. Fujisaki, T. Terada, T. Furuta, K. Moritsugu, A. Kidera, Minimum free energy path of ligand-induced transition in adenylate kinase. *PLOS Comput. Biol.* **8**, e1002555 (2012).
29. N. Juranic, E. Atanasova, A. G. Filoteo, S. Macura, F. G. Prendergast, J. T. Penniston, E. E. Strehler, Calmodulin wraps around its binding domain in the plasma membrane Ca^{2+} pump anchored by a novel 18-1 motif. *J. Biol. Chem.* **285**, 4015–4024 (2010).
30. J. Ådén, C. F. Weise, K. Brännström, A. Olofsson, M. Wolf-Watz, Structural topology and activation of an initial adenylate kinase-substrate complex. *Biochemistry* **52**, 1055–1061 (2013).
31. D. E. Koshland, Application of a theory of enzyme specificity to protein synthesis. *Proc. Natl. Acad. Sci. U.S.A.* **44**, 98–104 (1958).
32. O. Miyashita, J. N. Onuchic, P. G. Wolynes, Nonlinear elasticity, proteinquakes, and the energy landscapes of functional transitions in proteins. *Proc. Natl. Acad. Sci. U.S.A.* **100**, 12570–12575 (2003).
33. A. L. Watters, P. Deka, C. Correnti, D. Callender, G. Varani, T. Sosnick, D. Baker, The highly cooperative folding of small naturally occurring proteins is likely the result of natural selection. *Cell* **128**, 613–624 (2007).
34. Y. Shan, A. Arkhipov, E. T. Kim, A. C. Pan, D. E. Shaw, Transitions to catalytically inactive conformations in EGFR kinase. *Proc. Natl. Acad. Sci. U.S.A.* **110**, 7270–7275 (2013).
35. P. C. Whitford, O. Miyashita, Y. Levy, J. N. Onuchic, Conformational transitions of adenylate kinase: Switching by cracking. *J. Mol. Biol.* **366**, 1661–1671 (2007).
36. L. Rundqvist, J. Adén, T. Sparrman, M. Wallgren, U. Olsson, M. Wolf-Watz, Noncooperative folding of subdomains in adenylate kinase. *Biochemistry* **48**, 1911–1927 (2009).
37. J. Vincent, M. Andersson, M. Eklund, A. B. Wöhri, M. Odelius, E. Malmerberg, Q. Kong, M. Wulff, R. Neutze, J. Davidsson, Solvent dependent structural perturbations of chemical reaction intermediates visualized by time-resolved x-ray diffraction. *J. Chem. Phys.* **130**, 154502 (2009).
38. I. Josts, S. Niebling, Y. Gao, M. Levantino, H. Tidow, D. Monteiro, Photocage-initiated time-resolved solution x-ray scattering investigation of protein dimerization. *IUCrJ* **5**, 667–672 (2018).
39. T. W. Kim, S. J. Lee, J. Jo, J. G. Kim, H. Ki, C. W. Kim, K. H. Cho, J. Choi, J. H. Lee, M. Wulff, Y. M. Rhee, H. Ihee, Protein folding from heterogeneous unfolded state revealed by time-resolved x-ray solution scattering. *Proc. Natl. Acad. Sci. U.S.A.* **117**, 14996–15005 (2020).
40. L. Henry, M. R. Panman, L. Isaksson, E. Claesson, I. Kosheleva, R. Henning, S. Westenhoff, O. Berntsson, Real-time tracking of protein unfolding with time-resolved x-ray solution scattering. *Struct. Dyn.* **7**, 054702 (2020).

41. M. C. Thompson, B. A. Barad, A. M. Wolff, H. S. Cho, F. Schotte, D. M. C. Schwarz, P. Anfinrud, J. S. Fraser, Temperature-jump solution x-ray scattering reveals distinct motions in a dynamic enzyme. *Nat. Chem.* **11**, 1058–1066 (2019).
42. M. Cammarata, M. Levantino, F. Schotte, P. A. Anfinrud, F. Ewald, J. Choi, A. Cupane, M. Wulff, H. Ihee, Tracking the structural dynamics of proteins in solution using time-resolved wide-angle x-ray scattering. *Nat. Methods* **5**, 881–886 (2008).
43. H. Takala, A. Björling, O. Berntsson, H. Lehtivuori, S. Niebling, M. Hoernke, I. Kosheleva, R. Henning, A. Menzel, J. A. Ihalainen, S. Westenhoff, Signal amplification and transduction in phytochrome photosensors. *Nature* **509**, 245–248 (2014).
44. A. Björling, O. Berntsson, H. Lehtivuori, H. Takala, A. J. Hughes, M. Panman, M. Hoernke, S. Niebling, L. Henry, R. Henning, I. Kosheleva, V. Chukharev, N. V. Tkachenko, A. Menzel, G. Newby, D. Khakhulin, M. Wulff, J. A. Ihalainen, S. Westenhoff, Structural photoactivation of a full-length bacterial phytochrome. *Sci. Adv.* **2**, e1600920 (2016).
45. O. Berntsson, R. P. Diensthuber, M. R. Panman, A. Björling, E. Gustavsson, M. Hoernke, A. J. Hughes, L. Henry, S. Niebling, H. Takala, J. A. Ihalainen, G. Newby, S. Kerruth, J. Heberle, M. Liebi, A. Menzel, R. Henning, I. Kosheleva, A. Möglich, S. Westenhoff, Sequential conformational transitions and α-helical supercoiling regulate a sensor histidine kinase. *Nat. Commun.* **8**, 284 (2017).
46. M. Andersson, E. Malmerberg, S. Westenhoff, G. Katona, M. Cammarata, A. B. Wöhri, L. C. Johansson, F. Ewald, M. Eklund, M. Wulff, J. Davidsson, R. Neutze, Structural dynamics of light-driven proton pumps. *Structure* **17**, 1265–1275 (2009).
47. E. Malmerberg, Z. Omran, J. S. Hub, X. Li, G. Katona, S. Westenhoff, L. C. Johansson, M. Andersson, M. Cammarata, M. Wulff, D. van der Spoel, J. Davidsson, A. Specht, R. Neutze, Time-resolved WAXS reveals accelerated conformational changes in iodoretinal-substituted proteorhodopsin. *Biophys. J.* **101**, 1345–1353 (2011).
48. E. Malmerberg, P. H. M. Bovee-Geurts, G. Katona, X. Deupi, D. Arnlund, C. Wickstrand, L. C. Johansson, S. Westenhoff, E. Nazarenko, G. F. X. Schertler, A. Menzel, W. J. de Grip, R. Neutze, Conformational activation of visual rhodopsin in native disc membranes. *Sci. Signal.* **8**, ra26 (2015).
49. H. Ravishankar, M. N. Pedersen, M. Eklund, A. Sitsel, C. Li, A. Duelli, M. Levantino, M. Wulff, A. Barth, C. Olesen, P. Nissen, M. Andersson, Tracking Ca^{2+} ATPase intermediates in real time by x-ray solution scattering. *Sci. Adv.* **6**, eaaz0981 (2020).
50. M. Andersson, J. Vincent, D. van der Spoel, J. Davidsson, R. Neutze, A proposed time-resolved x-ray scattering approach to track local and global conformational changes in membrane transport proteins. *Structure* **16**, 21–28 (2008).
51. S. J. Lee, Y. Kim, T. W. Kim, C. Yang, K. Thamilselvan, H. Jeong, J. Hyun, H. Ihee, Reversible molecular motional switch based on circular photoactive protein oligomers exhibits unexpected photo-induced contraction. *Cell Rep. Phys. Sci.* **2**, 100512 (2021).
52. Y. Lee, J. G. Kim, S. J. Lee, S. Muniyappan, T. W. Kim, H. Ki, H. Kim, J. Jo, S. R. Yun, H. Lee, K. W. Lee, S. O. Kim, M. Cammarata, H. Ihee, Ultrafast coherent motion and helix rearrangement of homodimeric hemoglobin visualized with femtosecond x-ray solution scattering. *Nat. Commun.* **12**, 3677 (2021).
53. M. Choi, J. G. Kim, S. Muniyappan, H. Kim, T. W. Kim, Y. Lee, S. J. Lee, S. O. Kim, H. Ihee, Effect of the abolition of intersubunit salt bridges on allosteric protein structural dynamics. *Chem. Sci.* **12**, 8207–8217 (2021).
54. M. Levantino, B. A. Yorke, D. C. F. Monteiro, M. Cammarata, A. R. Pearson, Using synchrotrons and XFELs for time-resolved x-ray crystallography and solution scattering experiments on biomolecules. *Curr. Opin. Struct. Biol.* **35**, 41–48 (2015).
55. M. Kovermann, C. Grundström, A. E. Sauer-Eriksson, U. H. Sauer, M. Wolf-Watz, Structural basis for ligand binding to an enzyme by a conformational selection pathway. *Proc. Natl. Acad. Sci. U.S.A.* **114**, 6298–6303 (2017).
56. A. Barth, K. Hauser, W. Maentele, J. E. T. Corrie, D. R. Trentham, Photochemical release of ATP from "caged ATP" studied by time-resolved infrared spectroscopy. *J. Am. Chem. Soc.* **117**, 10311–10316 (1995).
57. M. Andersson, A. N. Bondar, J. A. Freites, D. J. Tobias, H. R. Kaback, S. H. White, Proton-coupled dynamics in lactose permease. *Structure* **20**, 1893–1904 (2012).
58. F. Oradd, M. Andersson, Tracking membrane protein dynamics in real time. *J. Membr. Biol.* **254**, 51–64 (2021).
59. D. J. Heyes, S. J. O. Hardman, M. N. Pedersen, J. Woodhouse, E. De La Mora, M. Wulff, M. Weik, M. Cammarata, N. S. Scrutton, G. Schirò, Light-induced structural changes in a full-length cyanobacterial phytochrome probed by time-resolved x-ray scattering. *Commun. Biol.* **2**, 1 (2019).
60. O. Berntsson, R. Rodriguez, L. Henry, M. R. Panman, A. J. Hughes, C. Einholz, S. Weber, J. A. Ihalainen, R. Henning, I. Kosheleva, E. Schleicher, S. Westenhoff, Photoactivation of *Drosophila melanogaster* cryptochrome through sequential conformational transitions. *Sci. Adv.* **5**, eaaw1531 (2019).
61. L. Henry, O. Berntsson, M. R. Panman, A. Cellini, A. J. Hughes, I. Kosheleva, R. Henning, S. Westenhoff, New light on the mechanism of phototransduction in phototropin. *Biochemistry* **59**, 3206–3215 (2020).
62. H. Ravishankar, A. Barth, M. Andersson, Probing the activity of a recombinant Zn^{2+} -transporting P-type ATPase. *Biopolymers* **109**, (2018).
63. A. Barth, W. Kreutz, W. Mäntele, Molecular changes in the sarcoplasmic reticulum calcium ATPase during catalytic activity. A Fourier transform infrared (FTIR) study using photolysis of caged ATP to trigger the reaction cycle. *FEBS Lett.* **277**, 147–150 (1990).
64. G. P. Hess, R. W. Lewis, Y. Chen, Caged neurotransmitters and other caged compounds: Design and application. *Cold Spring Harb. Protoc.* **2014**, pdb top084152 (2014).
65. P. Klán, T. Šolomek, C. G. Bochet, A. Blanc, R. Givens, M. Rubina, V. Popik, A. Kostikov, J. Wirz, Photoremovable protecting groups in chemistry and biology: Reaction mechanisms and efficacy. *Chem. Rev.* **113**, 119–191 (2013).
66. F. Zeller, M. Zacharias, Substrate binding specifically modulates domain arrangements in adenylate kinase. *Biophys. J.* **109**, 1978–1985 (2015).
67. E. Onuk, J. Badger, Y. J. Wang, J. Bardhan, Y. Chishti, M. Akcakaya, D. H. Brooks, D. Erdogmus, D. D. L. Minh, L. Makowski, Effects of catalytic action and ligand binding on conformational ensembles of adenylate kinase. *Biochemistry* **56**, 4559–4567 (2017).
68. A. Ansari, J. Berendzen, S. F. Bowne, H. Frauenfelder, I. E. Iben, T. B. Sauke, E. Shyamsunder, R. D. Young, Protein states and proteinquakes. *Proc. Natl. Acad. Sci. U.S.A.* **82**, 5000–5004 (1985).
69. D. Arnlund, L. C. Johansson, C. Wickstrand, A. Barty, G. J. Williams, E. Malmerberg, J. Davidsson, D. Milathianaki, D. P. DePonte, R. L. Shoeman, D. Wang, D. James, G. Katona, S. Westenhoff, T. A. White, A. Aquila, S. Bari, P. Berntsen, M. Bogan, T. B. van Driel, R. B. Doak, K. S. Kjær, M. Frank, R. Fromme, I. Grotjohann, R. Henning, M. S. Hunter, R. A. Kirian, I. Kosheleva, C. Kupitz, M. Liang, A. V. Martin, M. M. Nielsen, M. Messerschmidt, M. M. Seibert, J. Sjöhamn, F. Stellato, U. Weierstall, N. A. Zatsepin, J. C. H. Spence, P. Fromme, I. Schlichting, S. Boutet, G. Groenhof, H. N. Chapman, R. Neutze, Visualizing a protein quake with time-resolved x-ray scattering at a free-electron laser. *Nat. Methods* **11**, 923–926 (2014).
70. M. Levantino, G. Schirò, H. T. Lemke, G. Cottone, J. M. Glownia, D. Zhu, M. Chollet, H. Ihee, A. Cupane, M. Cammarata, Ultrafast myoglobin structural dynamics observed with an x-ray free-electron laser. *Nat. Commun.* **6**, 6772 (2015).
71. T. R. M. Barends, L. Foucar, A. Ardevol, K. Nass, A. Aquila, S. Botha, R. B. Doak, K. Falahati, E. Hartmann, M. Hilpert, M. Heinz, M. C. Hoffmann, J. Köfinger, J. E. Koglin, G. Kovacsova, M. Liang, D. Milathianaki, H. T. Lemke, J. Reinstein, C. M. Roome, R. L. Shoeman, G. J. Williams, I. Burghardt, G. Hummer, S. Boutet, I. Schlichting, Direct observation of ultrafast collective motions in CO myoglobin upon ligand dissociation. *Science* **350**, 445–450 (2015).
72. S. Geibel, A. Barth, S. Amslinger, A. H. Jung, C. Burzik, R. J. Clarke, R. S. Givens, K. Fendler, P3-[2-(4-hydroxyphenyl)-2-oxo]ethyl ATP for the rapid activation of the Na^+,K^+-ATPase. *Biophys. J.* **79**, 1346–1357 (2000).
73. M. Wulff, A. Plech, L. Eybert, R. Randler, F. Schotte, P. Anfinrud, The realization of sub-nanosecond pump and probe experiments at the ESRF. *Faraday Discuss.* **122**, 13–26 (2003).
74. M. Wulff, F. Schotte, G. Naylor, D. Bourgeois, K. Moffat, G. Mourou, Time-resolved structures of macromolecules at the ESRF: Single-pulse Laue diffraction, stroboscopic data collection and femtosecond flash photolysis. *Nucl. Instrum. Methods Phys. Res. A* **398**, 69–84 (1997).
75. H. S. Cho, F. Schotte, N. Dashdorj, J. Kyndt, R. Henning, P. A. Anfinrud, Picosecond photobiology: Watching a signaling protein function in real time via time-resolved small- and wide-angle x-ray scattering. *J. Am. Chem. Soc.* **138**, 8815–8823 (2016).
76. D. Svergun, C. Barberato, M. H. J. Koch, CRYSOL—A program to evaluate x-ray solution scattering of biological macromolecules from atomic coordinates. *J. Appl. Crystallogr.* **28**, 768–773 (1995).
77. S. Jo, T. Kim, V. G. Iyer, W. Im, CHARMM-GUI: A web-based graphical user interface for CHARMM. *J. Comput. Chem.* **29**, 1859–1865 (2008).
78. M. J. Abraham, T. Murtola, R. Schulz, S. Páll, J. C. Smith, B. Hess, E. Lindahl, GROMACS: High performance molecular simulations through multi-level parallelism from laptops to supercomputers. *SoftwareX* **1-2**, 19–25 (2015).
79. R. B. Best, X. Zhu, J. Shim, P. E. M. Lopes, J. Mittal, M. Feig, A. D. MacKerell Jr., Optimization of the additive CHARMM all-atom protein force field targeting improved sampling of the backbone ϕ, ψ and side-chain χ1and χ2 dihedral angles. *J. Chem. Theory Comput.* **8**, 3257–3273 (2012).
80. S. Nosé, A unified formulation of the constant temperature molecular dynamics methods. *J. Chem. Phys.* **81**, 511–519 (1984).
81. W. Hoover, Canonical dynamics: Equilibrium phase-space distributions. *Phys. Rev. A* **31**, 1695–1697 (1985).
82. M. Parrinello, A. Rahman, Polymorphic transitions in single crystals: A new molecular dynamics method. *J. Appl. Phys.* **52**, 7182–7190 (1981).
83. J. C. D. Houtman, P. H. Brown, B. Bowden, H. Yamaguchi, E. Appella, L. E. Samelson, P. Schuck, Studying multisite binary and ternary protein interactions by global analysis of isothermal titration calorimetry data in SEDPHAT: Application to adaptor protein complexes in cell signaling. *Protein Sci.* **16**, 30–42 (2007).
84. D. G. Rhoads, J. M. Lowenstein, Initial velocity and equilibrium kinetics of myokinase. *J. Biol. Chem.* **243**, 3963–3972 (1968).

85. S. Burlacu-Miron, V. Perrier, A. M. Gilles, J. Mispelter, O. Bârzu, C. T. Craescu, 1H, 13C and 15N backbone resonance assignment of Escherichia coli adenylate kinase, a 23.6 kDa protein. *J. Biomol. NMR* **13**, 93–94 (1999).
86. E. Meirovitch, M. A. Sinev, E. V. Sineva, Sequence-specific 1H, 15N and 13C assignment of adenylate kinase from *Escherichia coli* in complex with the inhibitor AP5A. *J. Biomol. NMR* **13**, 195–196 (1999).

Acknowledgments: We acknowledge the Swedish NMR Centre at Umeå University and the Knut and Alice Wallenberg foundation program "NMR for Life" and SciLifeLab for NMR support. The computations were performed on resources provided by the Swedish National Infrastructure for Computing (SNIC) through the High-Performance Computing Center North (HPC2N) under projects SNIC 2019/2-29 and SNIC 2020/5-684. We acknowledge the ESRF for provision of synchrotron radiation facilities and access to the ID09 beamline where the TR-XSS measurements were performed. **Funding:** This study was supported by the Swedish Research Council (grant 2017-04203 to M.W.-W.) and the Swedish Research Council (grant 2020-03840 to M.A.) **Author contributions:** Conceptualization: M.A. Methodology: F.O., H.R., J.G., P.R., L.B., A.D., M.N.P., M.L., M.W., M.W.-W., and M.A. Investigation: F.O., H.R., M.W.-W., and M.A. Visualization: F.O., H.R., P.R., L.B., M.W.-W., and M.A. Supervision: M.W.-W. and M.A. Writing—original draft: F.O., H.R., M.W.-W., and M.A. Writing—review and editing: All authors **Competing interests:** The authors declare that they have no competing interests. **Data and materials availability:** All data needed to evaluate the conclusions in the paper are present in the paper and/or the Supplementary Materials. The MD trajectories can be found at https://doi.org/10.5281/zenodo.5583119.

Submitted 17 March 2021
Accepted 27 September 2021
Published 17 November 2021
10.1126/sciadv.abi5514

ScienceAdvances

Tracking the ATP-binding response in adenylate kinase in real time

Fredrik OräddHarsha RavishankarJack GoodmanPer RogneLars BackmanAnnette DuelliMartin Nors PedersenMatteo LevantinoMichael WulffMagnus Wolf-WatzMagnus Andersson

Sci. Adv., 7 (47), eabi5514. • DOI: 10.1126/sciadv.abi5514

Science Advances (ISSN) is published by the American Association for the Advancement of Science. 1200 New York Avenue NW, Washington, DC 20005. The title *Science Advances* is a registered trademark of AAAS.